ARID ZONE JOURNAL OF ENGINEERING, TECHNOLOGY & ENVIRONMENT
AZOJETE June 2022. Vol. 18(2):255-266
Published by the Faculty of Engineering, University of Maiduguri, Maiduguri, Nigeria.
Print ISSN: 1596-2644, Electronic ISSN: 2545-5818
www.azojete.com.ng

ORIGINAL RESEARCH ARTICLE

APPLICATION OF SEM/EDS IN FRACTOGRAPHIC INVESTIGATION OF TIG WELDED AISI 1020 FUSION ZONES AT DISTINCT WELDING CURRENT STEPS

I. B. Owunna[1], A. E. Ikpe[2] and J. U. Ohwoekevwo[1]
[1]*Department of Mechanical Engineering, University of Benin, Benin City, Nigeria, P.M.B. 1154*
[2]*Department of Mechanical Engineering, Akwa Ibom State Polytechnic, Ikot Osurua, Ikot Ekpene, Nigeria, P.M.B. 1200*
**Corresponding author's email address: aniekan.ikpe@eng.uniben.edu*

ARTICLE INFORMATION

Submitted 11 October, 2021
Revised 7 March, 2022
Accepted 16 March, 2022

Keywords:
Welding
Low carbon steel
Welding current
TIG welding
Mechanical Properties

ABSTRACT

Higher arc length is a function of increasing welding current (amperage). It increases the intensity of welding heat, thereby, influencing the microstructure and mechanical properties of the welded material. In this this study, fractographical variations in TIG welded AISI 1020 fusion zones at different welding current steps were investigated using Scanning Electron Microscopy with Energy Dispersive Spectroscopy (SEM/EDS) techniques. The fracture morphologies showed a fibrous appearance indicating ductile fracture with initiation of a river pattern of branching cracks, forming cleavages along the crystals plains and intergranular fracture occurring along the grain boundaries, indicating brittle fracture as a result of stepwise increase in welding current. It was observed that the ultimate tensile strength of the welded samples decreased correspondingly from 583.3 MPa, 540 MPa, 530.7 MPa, 506.7 MPa to 473.3 MPa as the resulting heat input due to welding current increased from 96.14 A, 120 A, 155 A, 190 A to 213 A. This indicated that the lowest welding current (96.14A) produced fusion zone with the highest ductility when compared to other welding currents which produced fusion zones that tended to be brittle as a result of increasing heat inputs. It was observed that fusion zone with the lowest welding current showed the appearance of a fibrous structure produced by stretching of crystals in their lattice during heat application. Micro-hardness on the surface of the welds revealed that hardness increased with increase in welding current. Therefore, proper control measures should be put in place to ensure that welding input parameters are optimum.

1.0 Introduction

Tungsten Inert Gas (TIG) welding is one of the welding methods applied in the fusion process of two or more metals. It plays a significant role in welding of mild steel or thin sections of non-ferrous metals such as copper alloys, aluminium alloys, magnesium and stainless steel. TIG welding also referred to as Gas Tungsten Arc Welding (GTAW) is an electric arc welding process that employs a non-consumable tungsten electrode in the fusion process of metals (Owunna and Ikpe, 2018a; Owunna and Ikpe, 2019a). Welding current is the electrical amperage in the power equipment used in carrying out welding operation. It is usually read from the power meter, which provides the welding technician with information on the welding amperage or amount of current used. Welding current is one of the most influential welding parameter in welding operation because it has a high tendency of affecting bead geometry, electrode melting rate, deposition rate, heat affected zone and weld penetration depth (Ikpe et al., 2017). For example, Owunna et al. (2018) carried out a temperature and time dependent analysis on AISI 1020 Low Carbon Steel Plate of 10 mm thickness. The result revealed that at each increasing time step and welding

current, the heat distribution characterized by intense heat, phase transformation and alteration in mechanical properties gradually formed a spiral transient patterns from the weldment known as Heat Affected Zone (HAZ). Continuous increase in welding current (amperage) is reported to be characterized by higher arc length and intense heat which may alter the elemental composition, mechanical properties as well as the microstructure of the HAZ and fusion zones. Rajakuma et al. (2017) employed TIG welding process in the joining process of stainless steel pipe, and the heat transfer behaviour for various welding input was analysed. It was observed that the amplitude of transient temperature distribution increased alongside the heat input while the microstructure of the weld bead profile consisted of austenite and δ-ferrite in the fusion zone. The presence of ferrite reduced the hot cracking susceptibility during solidification of the molten weld. The effect of welding current (96.1- 213.8A) on elemental composition, mechanical properties and microstructure was demonstrated by Owunna and Ikpe (2019b) who employed Artificial Neural Network (ANN) and experimental approach in modelling and prediction of the mechanical properties of TIG welded joint for AISI 4130 low carbon steel plates. Optimized ANN predicted output parameters where UTS of 421 MPa, modulus of elasticity of 793 MPa, strain of 0.61 and elongation of 61% while experimental values using the optimized input variables produced output parameters of 427 MPa for UTS of 421 MPa, 806 MPa for modulus of elasticity, strain of 0.62 and 62% elongation. Visuals of the weldment obtained from Scanning Electron Microscopy with Energy Dispersive Spectroscopy (SEM/EDS) revealed a uniformly distributed grain sizes in the weldment primarily composing of iron (Fe), chromium (Cr), molybdenum (Mo), nickel (Ni) and manganese (Mn). This correlates with similar studies where GTAW was applied on 2mm thickness of Duplex Stainless Steel (DSS) and hot rolled medium and high Tensile Structural Steel. Scanning Electron Microscope (SEM) fractography analysis indicated that the weldments possessed good tensile strength without decrease in ductility of the fusion zone while elements like Si and Cr were also observed in the metallurgical properties (Devakumar et al., 2016). The chromium, silicon and molybdenum represents ferritic microstructure while nickel (Ni), manganese (Mn) represents austenitisers (Devakumar et al., 2015; Pawan and Nishant, 2013; Chern et al., 2011). SEM/EDS is a type of electron microscope that produces photographs of sample by scanning through the welded surface with a focused beam of electrons that interact with atoms within the welded rehion, generating numerous signals with details about the surface topography and composition of the sample. Hence, images that show the topography of the surface is created through the process of scanning the sample or the welded point and collecting the secondary electrons that are emitted using a special detector. In other words, SEM is the imaging part of the technique while the "regular" optical microscope utilizes light for imaging. Optical microscope and electron probe microanalysis (EPMA) approach were employed by Liu et al. (2004) to investigate the weldability and microstructure of AZ31B magnesium alloy using hybrid laser TIG welding, laser beam welding and TIG welding. In the fusion zone of hybrid laser TIG welding, equiaxed grains was observed which were smaller in sizes than the grain sizes obtained from TIG welding but larger than those obtained from laser beam welding. Huang et al. (2016) used GTAW multi-pass welding method to weld two dissimilar metals (S355JR carbon steel and 316L stainless steel plates), and consequently investigated the microstructural characteristics, mechanical properties and corrosion behaviour of the welded dissimilar joint. The results obtained revealed that the microstructure of the weldment was a combination of austenite and vermiform δ-ferrite. There was decarburisation layer on the interface of S355JR whereas, the damaged phase σ and $M_{23}C_6$ (chromium carbide) were not observed in the X-ray diffraction. In addition, the corrosion resistance of the weldment decreased when compared to 316L base material. In recent times, a number of computer aided tools such as Particle Swarm Optimization (PSO) algorithm, Artificial Neural Network (ANN), Response Surface methodology (RSM) and others have been employed in the prediction and optimization of welding parameters (Owunna and Ikpe; 2018b). However, only a few of these conventional techniques are applicable to investigations on

Corresponding author's e-mail address: aniekan.ikpe@eng.uniben.edu

material surface analysis and material failure, as they are mostly determined experimentally. This study is focused on investigation of fractographical variations in TIG welded AISI 1020 fusion zones at different welding current steps using SEM/EDS.

2. Materials and Methods

2.1. Materials

In this study, a series of AISI 1020 low carbon steel weldments were produced by TIG welding process. Table 1 indicated the materials and specifications used for the welding process.

Table 1: Materials and specifications used for the welding experimentation

S/N	Material Specification	Welding Specification
1	Welding Type	Tungsten Inert Gas (TIG)
2	Material	AISI 1020 Low Carbon Steel Plate
7	Material Thickness	10 mm
8	Filler Material	ER 70 S-6
9	Joint Type	Butt Joint (V-groove)
10	Joint Preparation	Abrasive Clean (Sand paper)/Acetone Wipe
11	Joint Gap	2 mm
12	Welding Current	D.C.E.N (Direct Current Electrode Negative)
13	Pulse Width	0.8 Seconds
14	Filler Rod Angle	15°
15	Welding Torch Angle	45°
16	Fixed Frequency	60Hz
17	Torch Type	Pro-torch (TIG Torch)
18	Tungsten Type	2% thoriated
19	Tungsten Size	3/1326" Diameter x 25.4 mm
20	Torch Gas	Argon (100%)
21	Heat Input Ratio	10.75 KJ/min
22	Weight of Filler Rod	78.5 Kg/m^2
23	Welding machine	Dynasty 210 DX
24	Clamp type	G-clamp for clamping the work pieces
25	Vertical milling machine	For milling the V-groove angle
26	Tensile machine	Instron
27	Welding spatter blanket	Non-asbestos woven glass fabric
28	Fire extinguisher	PP3P lightweight ABC dry powder
29	Hand gloves and helmet	For safety purpose

2.2. Methods

AISI 1020 low carbon steel plate (0.19% C, 0.25% Si, 0.4% Mn, 0.025% P, 0.015% S, 0.09% Al, 0.009% Mn, 0.05% Nb and 0.03% Ti) of 10 mm thickness each was cut into 60x20 mm (length x width) dimension as shown in Figure 1. Emery paper (coarse: P24 grit size with 715 µm and fine: P80 grit size with 201 µm) was used to smoothen and eliminate rough particles and rust from the surface of specimen before welding the samples in Figure 1. This was followed by cleaning the surface of the samples to be welded with acetone in order to eliminate surface contamination. Using vertical milling machine, the two steel plates were chamfered (2mm depth) with 30 degrees at the edge to form a V-groove angle while clamping it to a G-clamp. TIG welding was applied to join the plates and filling the chaffered region using 2% thoriated tungsten electrode. This was achieved through the use of Dynasty 210 DX welding machine and 100 % Argon as the torch gas to protect the welding region from contaminants. The TIG welding input variables

Corresponding author's e-mail address: aniekan.ikpe@eng.uniben.edu

employed in the welding process are presented in Table 2 while samples of the steel plates subjected to welding are shown in Figure 1.

Table 2: Design of experiment for TIG input variables

Weld Runs	Current (A)	Voltage (V)	Gas Flow Rate (L/min)
1	155	22	15.5
2	120	25	18
3	96.14	22	15.50
4	190	19	13
5	213	22	15.50

Figure 1: Samples of the steel plates subjected to welding

The method of Owunna and Ikpe (2019b) was employed in this study, where each of the welded samples was subjected to SEM/EDS to check the mechanical properties and characterization of the weldment. The above input variables in Table 2 were employed in the TIG welding process to join the work piece together before being subjected to tensile test. Tensile test was conducted on the samples at room temperature using Universal Material Testing Machine with ISO 6892 standard at a load of 200kN. The test machine is manufactured by Jinan Kason testing equipment Co., Ltd, China, with model number WDW-200. The ends of the specimens were gripped in the machine and loads were applied until deformation occurred. This was used to calculate for the corresponding mechanical properties. The UTS test was conducted to determine the maximum resistance of the welded specimen to fracture under tension while the hardness test was conducted to determine the resistance of the welded specimen to penetration by a pyramidal, conical or spherical indenter. To achieve these two parameters, the welded sample was subjected to preliminary measurements for five specimen welded at different currents before the application of load and final measurement after the application of load.

Hardness testing was used to evaluate the hardness depth of the surface-hardened welds of AISI 1020 low carbon steel. Hardness across the welds were measured by micro-hardness tester using 2 kg load. This was done by making a series of hardness impressions from the edge of the cross sectioned samples towards the center. The hardness progression was graphically plotted and distance from the surface to the hardness limit was calculated. The UTS, strain, Modulus of elasticity, percentage elongation were calculated using Equations 1-4.

$$\text{UTS} = \frac{F}{A} \quad (1)$$

$$\text{Strain } \Sigma = \frac{DL}{L} \quad (2)$$

Corresponding author's e-mail address: aniekan.ikpe@eng.uniben.edu

$$\% \text{ Elongation} = \frac{DL}{L} \times 100 \quad (3)$$

$$E = \frac{UTS}{\Sigma} \quad (4)$$

3. Results and Discussion

Figure 2 shows the microstructural view of the control sample investigated in this paper. Typical microstructure of the control sample is composed largely of equiaxed ferrite grains and small regions of pearlite (α-Fe + Fe_3C) at grain boundaries edges and corners.

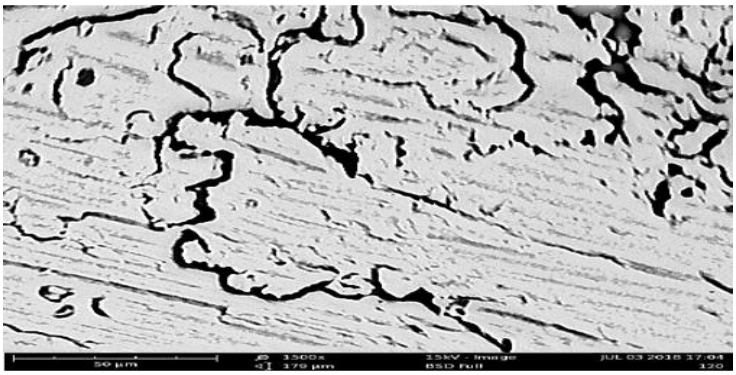

Figure 2: SEM image of control sample of the base metal with magnification of 1500X

As shown in Figure 2, there are evenly distributed fine grain ferrite (white), which exert decisive influence on cleavage fracture and dispersedly observed pearlite grains (gray). According to Chen and Cao (2015), it is possible that for some ferrite-perlite microstructure with similar patterns and grains of pearlite colonies, cracks are initiated in perlite colonies. However, the propagation of a pearlite-colony-sized cracks controls the cleavage fracture. It is clear that, the susceptibility to cleavage fracture does not solely depend on the size of the fracture-initiating particle but also on the local ferrite grain size. The average ferrite grain size could not be measured quantitatively as a result of "Widmanstatten" type microstructure observed. Additionally, few river-like patterns of branching cracks of ferrite and pearlite structures which contributes to the hardness of the material. Therefore, increase in pearlite grains would amount to increase in hardness (Maalekian, 2007; Malik et al., 2014), causing the material to be brittle. Figure 3 represents the topography of sample welded at a current of 96.14A and magnifications of 500-1500. For samples welded with low welding current, the bands of perlite-rich area (banding) were observed. Macro-segregation phenomenon known as banding, is due to the presence of high percentage of Mn (0.4-0.5%) in these regions. In more alloyed weld metals, elements such as chromium and molybdenum can be found to be segregated in these areas (Lars-Eric, 1994).

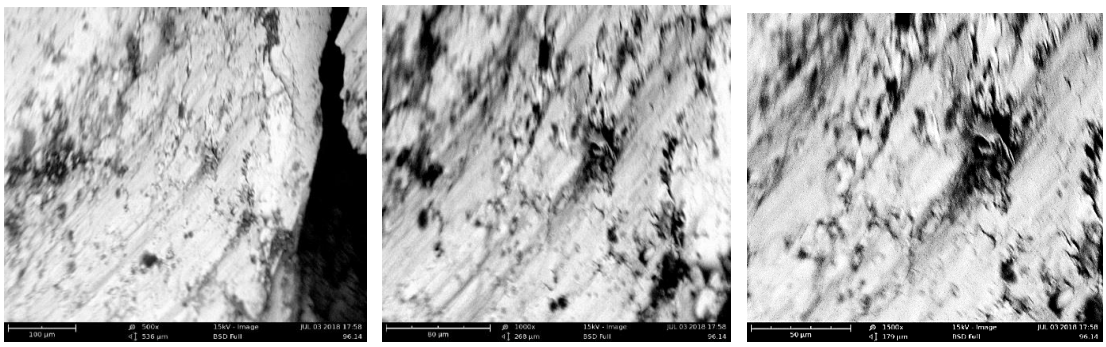

(a) **(b)** **(c)**

Figure 3: SEM images of the fusion zone welded at 96.14A with magnifications of (a) 500X, (b) 1000X,

(c) 1500X

Topography of samples at welding current of 96.14A, showed a fibrous structure produced by stretching of crystals give rise to a number of tear ridges and dimples as a result of low heat inputs in the material. The fractured surface here is ductile at different magnifications of 500X, 1000X and 1500X. Figure 4 represents the topography of sample welded at a current of 120A and magnifications of 500-1500X.

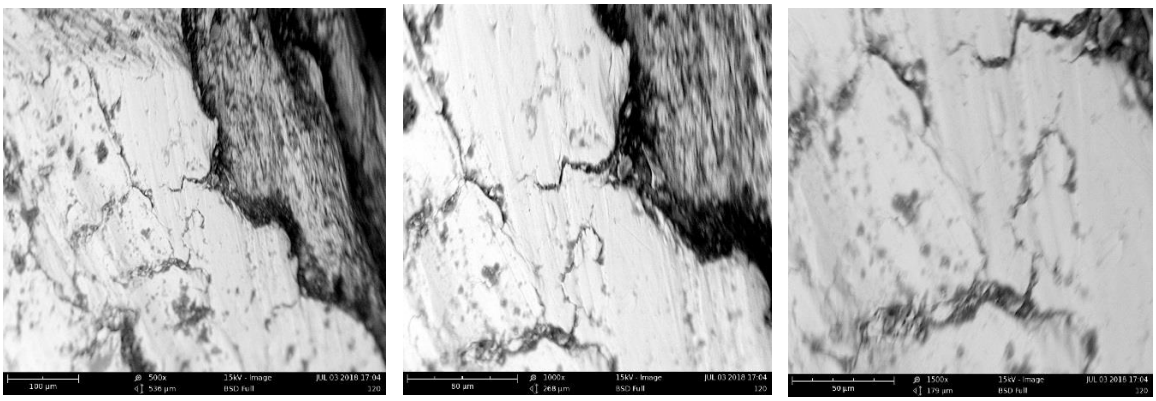

(a) **(b)** **(c)**

Figure 4: SEM images of the fusion zone welded at 120A with magnifications of (a) 500X, (b) 1000X, (c) 1500X

Topography of sample welded at current of 120A, showing a mixed type of failures (fractures). The fractures show fibrous appearance indicating ductile fracture with initiation of a river pattern of branching cracks forming cleavages along the crystals plains and intergranular fracture occurring along the grain boundaries, indicating a brittle fracture as a result of welding heat inputs increase. Magnifications (500X, 1000X and 1500X) which the fusion zones were viewed after welding allows the fracture patterns to be seen clearly. Figure 5 represents the topography of sample welded at a current of 155A and magnifications of 500-1500X.

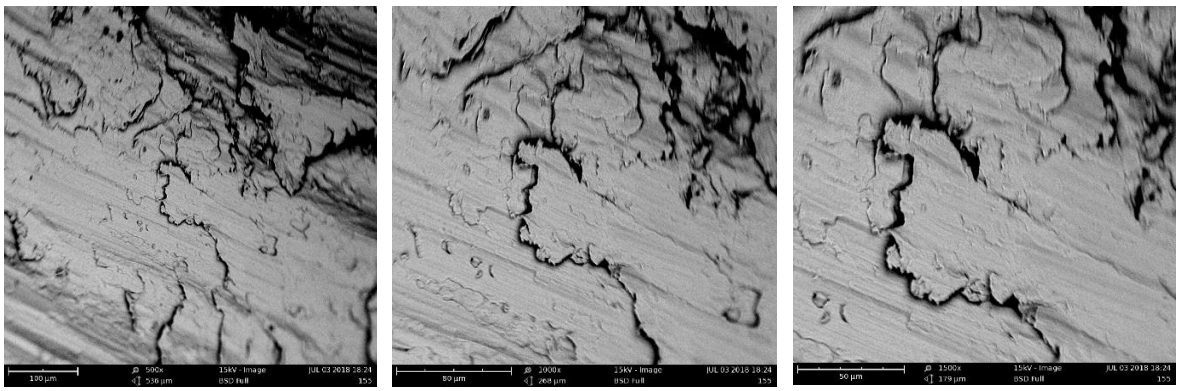

(a) **(b)** **(c)**

Figure 5: SEM images of the fusion zone welded at 155A with magnifications of (a) 500X, (b) 1000X, (c) 1500X

Topography of sample welded at a current of 155A, showed decrease in ductility. This occurred as a result of decrease in fibrous appearance with reduction in the number of tear ridges and dimples and an increase in cleavage steps of branching cracks and surfaces of inter-granular brittle fractures. The fracture here appears more brittle as a result of step increase in welding heat inputs. These properties on the fusion zone is different from the base metal, because it is also characterized by pseudo-grains and a microstructural inhomogeneity which is a result of fast cooling rates. It appears that the zone in Figure 6 mainly contains ferrite and some colonies of pearlite. Hence, the microstructure that evolved in the weld is heterogeneous due to the welding temperature gradients and the chemical reaction that evolved during

Corresponding author's e-mail address: aniekan.ikpe@eng.uniben.edu

the welding process (Grong, 1994). Figure 6 represents the topography of sample welded at a current of 190A and magnifications of 500, 1000 and 1500X.

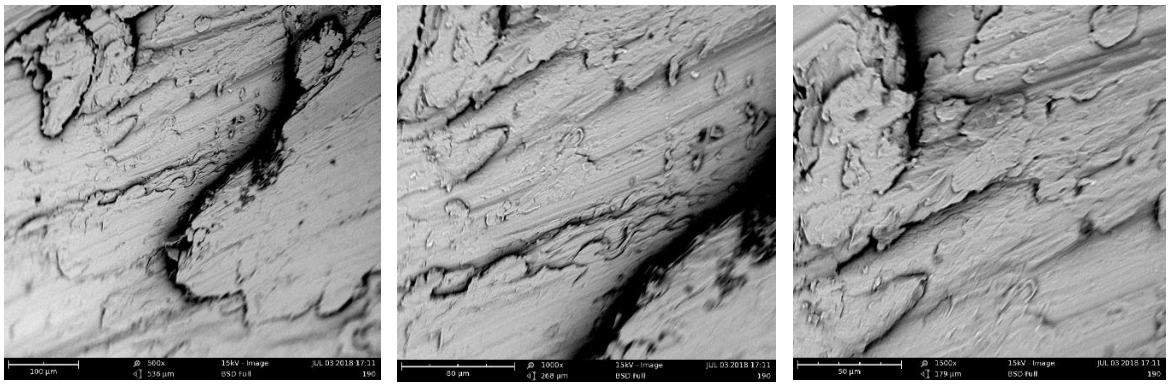

(a) **(b)** **(c)**

Figure 6: SEM images of the Fusion Zone Welded at 190A with Magnification of (a) 500X, (b) 1000X, (c) 1500X

Topography of sample welded at current of 190A, showing a stepwise increase in branching cracks of cleavage steps, Widmanstatten ferrite, and some colonies of pearlite along the grain boundaries. This agrees with the findings of Boumerzoug et al. (2010). The fractured surface appeared to be more brittle as heat input increased, causing reduction in ductility. In similar study, Ikeh et al. (2019) observed that the fracture surfaces showed dimples of varying sizes and shapes, indicating ductile (due to low arc heat) to brittle (due to high arc heat) fracture. Low arc heat (72 kJ/mm), showed a classic mechanism of ductile fracture known as micro-void coalescence. High arc heat (90 kJ/mm) showed trans-granular form of fracture which indicates brittle fracture in which the failure occurred with lower plastic deformation. Figure 7 represent the topography of sample welded at a current of 213A and magnifications of 500-1500X. It showed the effect of heat distribution on elongation of ferrite grains. Bayraktar et al. (2007) observed in interstitial free steels that the welded joints are characterized by the presence of very large grains near the fusion line and these grains are oriented along the regions with high heat distribution.

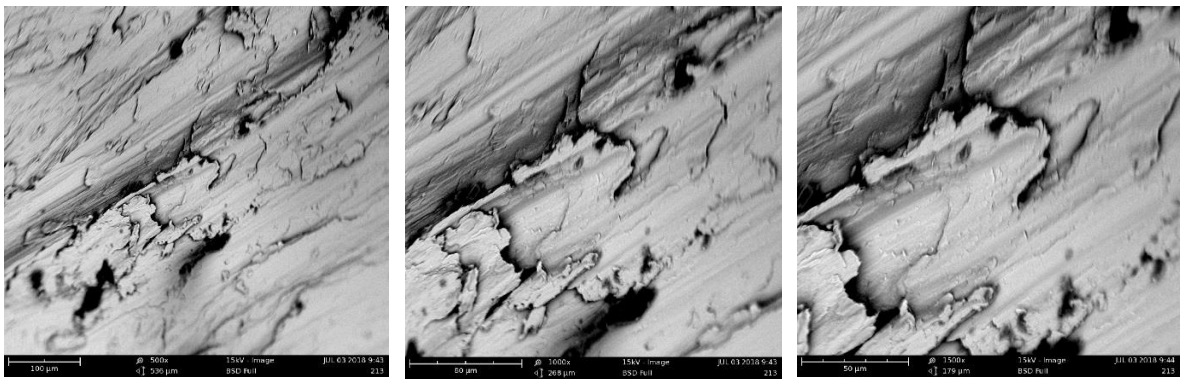

(a) **(b)** **(c)**

Figure 7: SEM images of the Fusion Zone Welded at 213A with Magnification of (a) 500X, (b) 1000X, (c) 1500X

Topography of sample welded at current of 213A, showing crystalline appearance indicating brittle fracture with river pattern of branching cracks and surfaces of inter-granular fracture occurring at grain boundaries. Brittle failure or fracture as mentioned in this context is the failure of a material without apparent plastic deformation. It occurs suddenly and the broken pieces can be fitted together to produce the original shape. The fracture may be in the form of cleavage along the crystal planes or it may be inter-granular,

occurring along the grain boundaries. Brittle fracture, characterised by fast crack propagation appears granular and glossy. Similarly, Plastic failure or ductile failure as mentioned in this study is a type of failure that involves considerable plastic deformation preceding the fracture. The material begins to neck beyond the ultimate tensile strength. Ductile material under static loading, plastic flow of materials precedes fracture and rupture surface shows a fibrous structure produced by the stretching of crystals giving rise to a number of tear ridges and dimples (Onyekpe, 2002).

3.1. Ultimate Tensile Strength and Micro-hardness of the Welds

Table 3 represents the measured values obtained from the welded samples, Table 4 results of Mechanical Properties while Figure 8 is a graphical view of Ultimate Tensile Strength (UTS) and elastic modulus of the welded samples at different welding temperature.

Table 3: Measured values of the welded samples

Sample	Width (mm)	Thickness (mm)	Load (KN)	Lo (mm)	LF (mm)
96.14A	30	10	142	60	62
120A	30	10	152	✓	60
155A	30	10	159.5	✓	62
190A	30	10	175	✓	62
213A	30	10	162	✓	60

Table 4 shows the results of mechanical properties of fusion zone of AISI 1020 welded with distinct current steps. It contains the UTS, strain, percentage elongation and young's modulus which were all derived from Equation 1-4. The mechanical properties as shown in Table 4 are the physical properties that the welded specimens exhibit upon the application of forces which tend to affect the geometry and performance of the welds when applied to structural members. The results of UTS and Modulus of elasticity of the welds presented in Table 4 are graphically plotted against welding currents employed in the fusion process as shown in Figure 8. Figure 8 shows that UTS decreases as welding current increases. The welding current in this case is considered as the arc heat because increase in welding current results in increase of the arc heat and vice versa. Furthermore, Figure 8 implied that Modulus of elasticity also decrease as welding current increased, but the rate of decrease was almost insignificant, possibly due to error in the readings, calculations or the welding process. The strain and percentage elongation were not graphically presented as there were no changes in the values throughout the welding current steps, indicating that the effect of welding current on strain or elongation property of welds is likely to be insignificant.

Table 4: Results of mechanical properties

Samples welded at different currents	UTS (MPa)	Σ Strain (mm/mm)	% Elongation (%)	E Young Modulus (MPa)
96.14	583.3	0.17	17	3.43117
120	540.0	0.17	17	3.17647
155	530.7	0.17	17	3.12747
190	506.7	0.17	17	2.98058
213	473.3	0.17	17	2.78412

Corresponding author's e-mail address: aniekan.ikpe@eng.uniben.edu

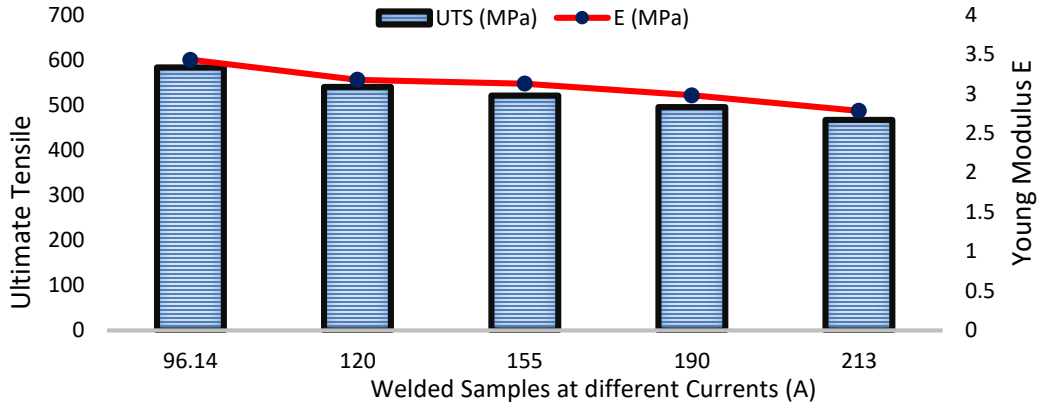

Figure 8: Graphical representation of UTS and elastic modulus

Figures 9a-e indicates the micro-hardness on the surface of the fusion zone, measured from the base metal across the weld metal after welding. The 60 mm shown on the plot represents the length of the welded samples while the distances ranging from 1-22 mm represents the indent spacing. After calculating the distance from the surface to the hardness limit, average was calculated from five points of micro-hardness on each weld produced by welding current of 96.14, 120, 155, 190 and 213 A.

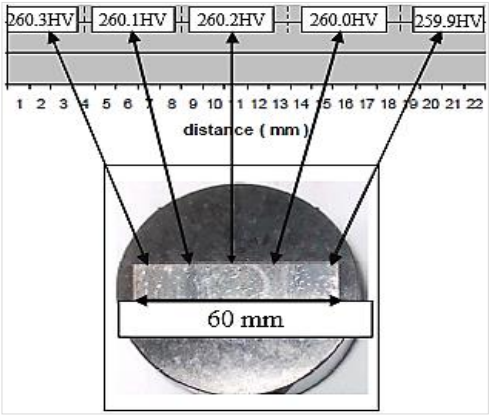

a. Welding current of 96.14 A

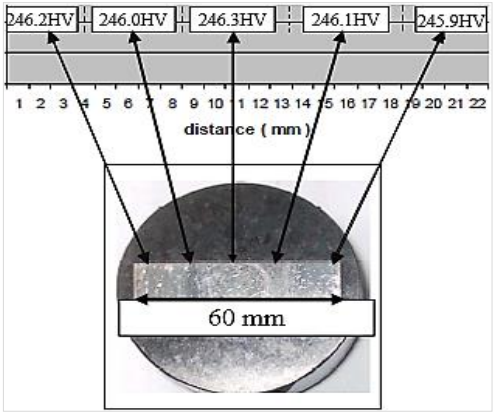

b. Welding current of 120 A

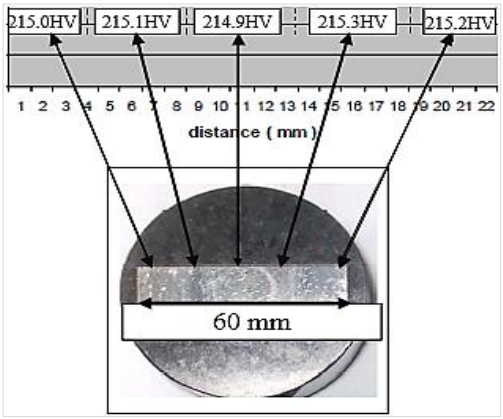

c. Welding current of 155 A

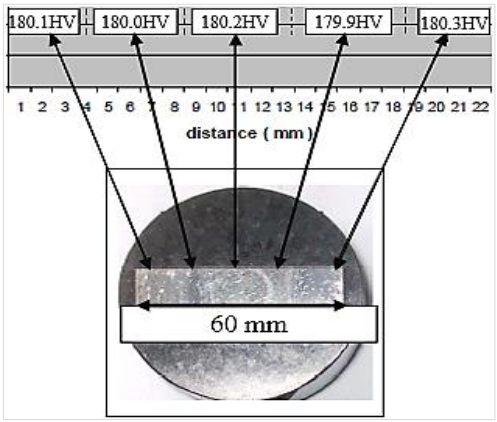

d. Welding current of 190 A

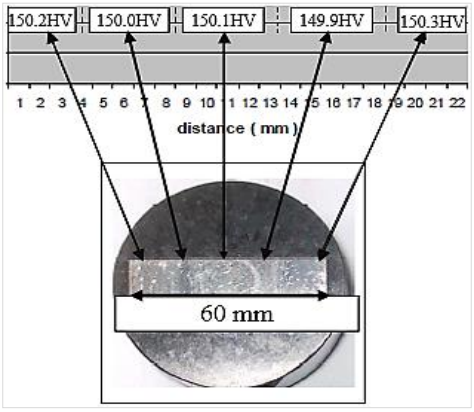

e. Welding current of 213 A

Figure 9: Micro-hardness on the surface of welds produced by different welding current

Average results of surface micro-hardness obtained from welds produced by TIG welding techniques using the aforementioned welding currents are presented in Figure 10. The result shown on the plot indicates that micro-hardness on welded joint increases as the welding current increased. Average hardness values obtained in this study using welding current from 96-213 ranged from 150.1-260.1 HV, whereas, hardness values obtained in similar studies conducted by Boumerzoug et al. (2010) ranged from 178-250 HV at locations within 1 mm from the welded metal, through the HAZ across the weld metal to the base plate. The increase in welding current during the welding process results in an increase of the arc heat which causes phase transformation in the fusion zone and after cooling, grains in the welded region becomes coarser with significant local embrittlement which reduces hardness performance of the welded steel material (Li et al., 2019). This correlated with the findings of Muda et al. (2015) who indicated that the higher the welding heat input, the coarser the microstructure. The phase transformations which occur in two phases may be high temperature transformation of δ-Fe to γ-Fe and transformation of γ-Fe to α-Fe (Dodo et al., 2016). Gharibshahiyan et al. (2011) found that slow cooling rate can also cause nucleation of coarse grain structures with high intergranular spacing which is characterised by reduction in hardness, thereby causing increase in grain dislocations within the crystal lattice of the fusion zone.

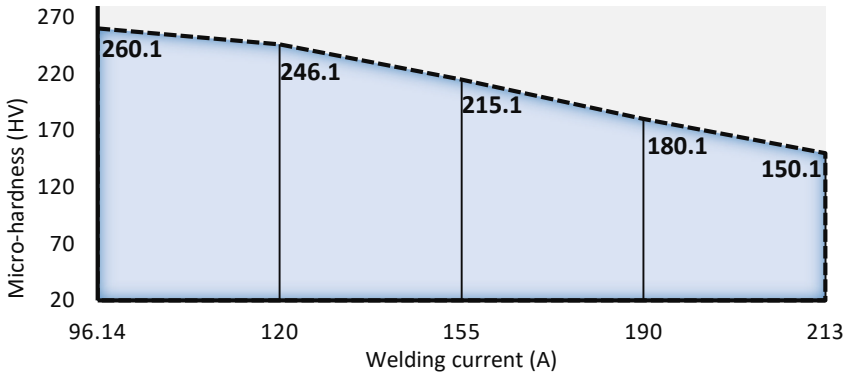

Figure 10: Average micro-hardness on the surface of welds produced by different welding current

4. Conclusion

All welds are prone to some level of defects, and it is more or less impossible to achieve a weld with zero defect. The phase transformation which occur from solid to semi-solid phase and from semi-solid phase to liquid phase depended largely on welding current. The phase transformation due to welding current is a function of welding temperature, heat input, type of material, cooling rate, welding parameters. At

Corresponding author's e-mail address: aniekan.ikpe@eng.uniben.edu

different welding current step applied in this study, fusion zones after solidification showed various fractured appearances such as river pattern of branching cracks, inter-granular fracture, ductile fracture and brittle fracture. It was also observed that the lowest current (96.14 A) employed in this investigation produced the highest UTS of 583.3 MPa and highest modulus of elasticity of 3.43117 MPa and vice versa. In this case, increased value of the modulus of elasticity signifies increase in the stiffness of the material as well as increase in the material tensile property. Micro-hardness on the surface of the welds revealed that hardness increased with decreasing welding current. Other factors such as grain size, welding current, arc heating also contribute to hardening of welded joints. Therefore, proper welding experiments should be performed to determine optimum welding current for a given material to avoid unwanted catastrophes.

References

Bayaraktar, E., Kaplan, D., Devillers, L. and Chevalier, JP. 2007. Grain Growth Mechanism during the Welding of Inter-stitial Free (IF) Steels. Journal of Materials Processing Technology, 189(1-3): 114-125.

Boumerzoug, Z., Derfouf, C. and Baudin, T. 2010. Effect of Welding on Microstructure and Mechanical Properties of an Industrial Low Carbon Steel. Engineering, 2: 502-506.

Chen, J. and Cao, R. 2015. Microorganism of Cleavage Fracture of Metals: A Comprehensive Microphysical Model for Cleavage Cracking in Metals, 1st Edition. Butterworth-Heinemann, Oxford, 1-486.

Chern, T., Tseng, K. and Tsai, H. 2011. Study of the Characteristics of Duplex Stainless Steel Activated Tungsten Inert Gas Welds. Materials and Design, 32(1): 255-263.

Devakumar, D., JabaraJ, DB. and Raja, VKB. 2015. Literature Review on the Effect of Processing on the Mechanical and Metallurgical Properties of Low Carbon Steels, Journal of Engineering and Applied Science, 10(11): 5012-5016.

Devakumar, D., JabaraJ, DB., Raja, VKB. and Jayaprakash, J. 2016. Experimental Investigation of DSS/HRS GTAW Weldments, Indian Journal of Science and Technology, 9(43): 1-6.

Dodo, MR., Ause, T., Adamu, MA. and Ibrahim, YM. 2016. Effect of Post-weld Heat Treatment on the Microstructure and Mechanical Properties of Arc Welded Medium Carbon Steel. Nigerian Journal of Technology, 35(2): 337-343.

Gharibshahiyan, E., Raouf, AH., Parvin, N. and Rahimian, M. 2011. The effect of Microstructure on Haerdness and Toughness of Low Carbon Welded Steel Using Inert Gas Welding. Material and Design, 32(4): 2042-2048.

Grong, O. 1994. Metallurgical Modelling of Welding. Materials Modelling Series. The Institute of Materials, Oxford, England.

Huang, BS., Yang, J., Lu, DH. and Bin, WJ. 2016. Study on the Microstructure, Mechanical Properties and Corrosion Behaviour of S355JR/316L Dissimilar Welded Joint Prepared by Gas Tungsten Arc Welding Multi-Pass Welding Process. Journal of Science and Technology of Welding and Joining, 21(5): 381-388.

Ikeh, OD., Ikpe, AE. and Njelle, VZ. 2019. Effects of Electric Power Arc Inputs on the Fracture Surface and the Mechanical Properties of 0.4%C Steel. Journal of Science and Technology Research, 1(3): 133-143.

Ikpe, AE., Owunna, I. and Ememobong, I. 2017. Effects of Arc Voltage and Welding Current on the Arc Length of Tungsten Inert Gas Welding (TIG). International Journal of Engineering Technologies, 3(4): 213-221.

Lars-Eric, S. 1994. Control of Microstructures and Properties in Steel Arc Welds. Library of Congress Cataloguing in Published Data, UK.

Li, D., Wu, K., Dong, H., Isayev, O. and Hress, O. 2019. Coarse Grained Heat-Affected Zone Microstructure and Brittleness of Ti-Nb-B Microalloyed High Toughness and Wear Resistant Steel. Metals, 9(3): 289-303

Corresponding author's e-mail address: aniekan.ikpe@eng.uniben.edu

Liu, LM., Wang JF. and Song, G. 2004. Hybrid Laser-TIG Welding Laser Beam Welding and Gas Tungsten Arc Welding of AZ31B Magnesium Alloy. Material Science and Engineering A, 381: 129-133.
Maalekian, M. 2007. The Effects of Alloying Elements on Steels (I). Graz Institute of Material Science, Joining and Forming (3030), Styria, Austria.
Malik, J., Toor, IH., Ahmed, WH., Gasem, ZM., Habib, MA., Ben-Mansour, R. and Badr, HM. 2014. Investigation on the Corosion-Enhanced Erosion Behaviour of Carbon Steel AISI 1020. International Journal of Electrochemical Science, 9: 6765-6780.
Muda, WS., Nasir, NS., Mamat, S. and Jamian, S. 2015. Effect of Welding Heat Input on Microstructure and Mechanical Properties at Coarse Grain Heat Affected Zone of ABS Grade A Steel. ARPN Journal of Engineering and Applied Sciences, 10(20): 9487-9495.
Owunna, IB. and Ikpe, AE. 2019a. Evaluation of induced residual stresses on AISI 1020 low carbon steel plate from experimental and FEM approach during TIG welding process. Journal of Mechanical Engineering and Sciences, 13(1): 4415-4433.
Owunna, I. and Ikpe AE. 2018b. Optimization of TIG Welding Input Variables for AISI 1020 Low Carbon Steel Plate Using Response Surface Methodology International Journal of Engineering Science and Application, 2(3): 113-122.
Onyekpe, B. 2002. The Essentials of Metallurgy and Materials in Engineering. AMBIK Press, Benin City, Nigeria.
Owunna, I., Ikpe, AE. and Achebo, JI. 2018. Temperature and Time Dependent Analysis of Tungsten Inert Gas Welding of Low Carbon Steel Plate using Goldak Model Heat Source. Journal of Applied Science and Environmental Management, 22(11): 1719-1725.
Owunna, IB. and Ikpe, AE. 2018a. Effects of Parametric Variations on Bead Width of Gas Tungsten Arc Welding of AISI 1020 Low Carbon Steel Plate. International Journal of Engineering Technology and Sciences, 5(3): 1-13.
Owunna, IB. and Ikpe, AE. 2019b. Modelling and Prediction of the Mechanical Properties of TIG Welded Joint for AISI 4130 Low Carbon Steel Plates Using Artificial Neural Network (ANN) Approach. Nigerian Journal of Technology 38(1): 117-126.
Pawan, KB. and Nishant, R. 2013. Parameters Optimization for gas metal arc welding of austenitic stainless steels and low carbon steel using Taguch's technique. International Journal of Engineering and Management Research, 3(4): 18-22.
Rajakuma, J., Bathusa, MS., Rajan, NP., Sulaiman, K., Christopher, AS. and Ganesh, I. 2017. Numerical Investigation of Heat Transfer Behavior during TIG Welding of Stainless Steel Pipes for Various Welding Heat Input Conditions. American Journal of Mechanical and Industrial Engineering, 2(3): 117-126

Corresponding author's e-mail address: aniekan.ikpe@eng.uniben.edu